PHYSICAL REVIEW E **67**, 051303 (2003)

Development of correlations in the dynamics of wet granular avalanches

P. Tegzes,[1,2] T. Vicsek,[2] and P. Schiffer[1]

[1]*Department of Physics and Materials Research Institute, Pennsylvania State University, University Park, Pennsylvania 16802*

[2]*Department of Biological Physics, Eötvös Loránd University, 1A Pázmány sétány, Budapest 1117, Hungary*

(Received 29 July 2002; published 14 May 2003)

A detailed characterization of avalanche dynamics of wet granular media in a rotating drum apparatus is presented. The results confirm the existence of the three wetness regimes observed previously: the granular, the correlated, and the viscoplastic regime. These regimes show qualitatively different dynamic behaviors that are reflected in all the investigated quantities. We discuss the effect of interstitial liquid on the characteristic angles of the material and on the avalanche size distribution. These data also reveal logarithmic aging and allow us to map out the phase diagram of the dynamic behavior as a function of liquid content and flow rate. Via quantitative measurements of the flow velocity and the granular flux during avalanches, we characterize avalanche types unique to wet media. We also explore the details of viscoplastic flow (observed at the highest liquid contents) in which there are lasting contacts during flow, leading to coherence across the entire sample. This coherence leads to a velocity independent flow depth at high rotation rates and robust pattern formation in the granular surface.

DOI: 10.1103/PhysRevE.67.051303 PACS number(s): 45.70.−n, 45.70.Ht

I. INTRODUCTION

While most research on the physics of granular media has focused on dry grains, the presence of even microscopic quantities of interstitial liquid can have profound effects on the physical behavior [1–11]. Capillary forces lead to cohesion between individual grains, which greatly enhances the stability of wet samples, and several recent studies have investigated liquid-induced effects on the static properties [4–9]. In previous studies of the repose angle of wet granular media using a draining crater apparatus [12], we identified three fundamental regimes as a function of the liquid content. The *granular regime* at very low liquid contents is dominated by the motion of individual grains; in the *correlated regime* corresponding to intermediate liquid contents, a rough surface is formed by the flow of separated clumps; and the repose angle of very wet samples results from smooth, cohesive flow in which the entire surface moves together. This regime is labeled as *viscoplastic* since the flow bears some resemblance to that of viscoplastic materials. The addition of liquid also qualitatively changes the dynamic behavior of granular media, as was observed qualitatively in our angle of repose measurements and also revealed in recent segregation studies [10,11]. A quantitative characterization of the *dynamics* of wet granular flow, however, has so far been missing. In this paper, we study the avalanche dynamics and flow properties of wet granular materials to investigate how the gradual addition of a small amount of liquid influences the dynamic properties of granular surface flow, and we find that the three fundamental regimes observed earlier are also reflected in the present experiment. Some of the results presented here have been published elsewhere [13].

Granular surface flow occurs when the inclined surface of a granular medium loses its stability against gravitational force. There are several experimental methods to investigate such flow, e.g., by gradually tilting a granular sample, which leads to an avalanche when the surface angle exceeds a critical value $\theta_{\max}$ [14]. Alternatively, if the surface angle is close to $\theta_{\max}$, avalanches can be triggered by pointlike perturbations [15]. The inclination of the surface can also be increased by the addition of grains to the top of the pile [16,17] or by slowly decreasing the size of the supporting base [18].

In our measurements, we employ a rotating drum apparatus (a cylindrical chamber partly filled with a granular medium and rotated around a horizontal axis) [19,20], which tilts the sample in a highly controlled and reproducible manner and offers several benefits. The most important advantage of a rotating drum is that at low rotation rates it allows for the observation of many avalanches without the need to change the sample. After each avalanche the medium remains at rest relative to the drum, while its surface angle is slowly increased by rotation until it reaches $\theta_{\max}$ again. Then another avalanche occurs, and the process starts over. Thus, it is possible to record hundreds of avalanches, which is essential for performing a statistical analysis or for averaging out noiselike fluctuations in dynamic data. In addition to the avalanches observed at low rotations rates, the rotating drum also allows the investigation of continuous flow down the slope at higher rotation rates.

The sections of this paper cover different aspects of our rotating drum experiments. We focus primarily on the macroscopic phenomena associated with the collective behavior of the grains, although the details of cohesion can also be studied at the microscopic level [1,2,4,6,10]. In Sec. II, we describe the experimental setup. Section III addresses some issues explored in previous studies of cohesive granular media in a rotating drum [8,21–23], focusing on the surface angles of the medium before and after avalanches, and describing a statistical analysis of avalanche size based on these angles. In Sec. IV, we investigate the transition between avalanches and continuous flow as a function of the liquid content, and map out the phase diagram of the system. Then Sec. V is devoted to the morphology of the surface. In the rest of the paper, we focus on characterizing the *dynamics of cohesive flow*. In Sec. VI, we quantitatively investigate the flow dynamics during avalanches at different liquid con-

1063-651X/2003/67(5)/051303(17)/$20.00

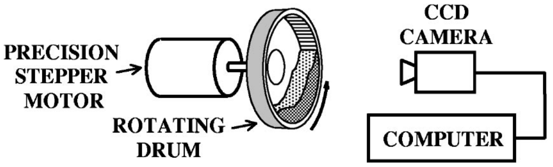

FIG. 1. Sketch of the experimental setup.

tents by analyzing the time evolution of the averaged surface profile obtained from hundreds of avalanche events. In Sec. VII, we analyze the dynamic properties of the continuous flow phase occurring at faster rotation. We pay special attention to the nature of the *viscoplastic* flow observed at the highest liquid contents, which displays unique characteristics associated with coherent motion over the entire granular surface. In the final section, we summarize and discuss our results.

II. DESCRIPTION OF THE APPARATUS

We studied glass spheres thoroughly mixed with small quantities of hydrocarbon oil. The viscosity of the oil used was 0.027 $\mathrm{N\,m^{-2}\,s}$, and its surface tension was 0.02 N/m. The liquid content varied between $\tau = 0.001\%$ and 5% of the void volume. In this regime, the flow of oil due to gravity can be neglected. Measurements were performed on three sizes of beads with diameters $d = 0.9\ \mathrm{mm} \pm 11\%$, $d = 0.5\ \mathrm{mm} \pm 20\%$, and $d = 0.35\ \mathrm{mm} \pm 15\%$. Note that the beads differed not only in their size, but also presumably in their microscopic surface structures, which are difficult to characterize or control. Nonetheless, most of the qualitative behavior is reproduced in the different grain samples, and the differences that are significant are mentioned below.

The rotating drum (Fig. 1) was made of thick plexiglas, but the vertical walls were lined with glass plates in order to minimize electrostatic effects. To prevent slips along the circumference of our drum, we inserted a hollow, thin aluminum cylinder with a rough inner surface into the drum. The inner diameter of the drum was 16.8 cm, its width was 3.2 cm, and the granular filling was 30%. By performing measurements in a thinner (2 cm) drum we verified that, while wall effects are not negligible, they do not appear to modify the qualitative behavior.

The drum was rotated by a computer-controlled precision stepping motor that provided an extremely stable rotation rate that could be varied in the range of $\approx 0.003-30$ rotation per minute (rpm). The step size of rotation was 0.025°. The vibrations originating from the stepper motor were damped by multiple lead bricks attached to the apparatus.

The experiment was recorded by a charge coupled device video camera interfaced to a computer that could analyze the spatiotemporal evolution of the surface profile (height variations in the axial direction were negligible). The steps of image processing are demonstrated in Figs. 2(a)–2(c). When the grains are wet, the beads sticking to the glass walls obscure the top surface of the grains [Fig. 2(a)]. We overcame this problem by using background illumination [Fig. 2(b)] and applying a brightness threshold [Fig. 2(c)] to the image.

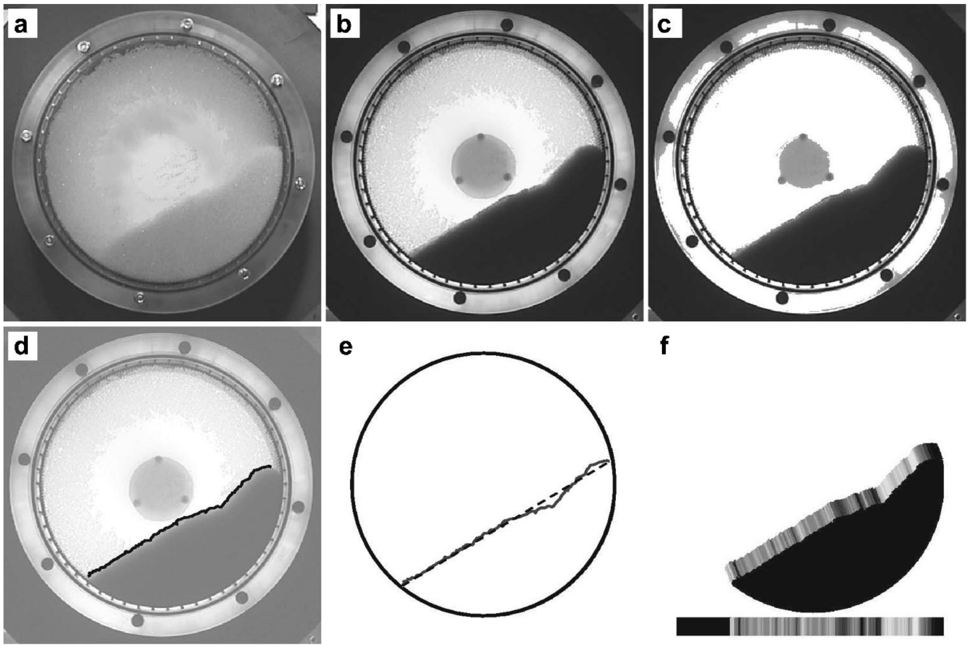

FIG. 2. Steps of image processing. (a) Snapshot taken without background illumination. The wet grains sticking to the glass walls make the surface profile hardly visible. (b) The same picture but with a circular lamp illuminating the background. In diffuse background illumination, the monolayer of beads on the wall is much brighter than the 3.2 cm-thick sample. (c) A brightness threshold is applied to the image to make the beads on the walls disappear. (d) Test of the algorithm: the surface data (black line) superimposed over a gray version of the original photograph. (e) The surface profile with a fitted straight line determining the overall surface angle θ. (f) Pseudo-three-dimensional representation of the surface profile, shading indicates local angle $\alpha(x)$. This shading may be used to represent a given surface profile in a single line (see the horizontal stripe at the bottom).

We found the surface profile $h(x)$ by an algorithm based on the detection of points of maximum contrast [24]. The resulting surface data are presented in Figs. 2(d)–2(f) in different ways. Figure 2(d) shows a test of the algorithm: the detected surface is superimposed on the photograph of the system as a thin black line. The limitations of our camera and computer gave us a resolution of $\delta t = 0.03$ s and $\delta x = 0.5$ mm. Figure 2(e) presents the $h(x)$ curve together with a straight line that was fitted to the curve in a rotation-invariant way: the squared sum of the *geometrical distances* of the surface point from the line was minimized. The inclination angle of this line gives the *overall angle* of the surface. This is the generalized version of the surface angle that has typically been used to describe the flat surface of dry samples. Finally, Fig. 2(f) shows the surface profile with a brightness-coded representation of the local angle ($\alpha(x) = \arctan[\partial_x h(x)]$) in the third dimension. The stripe at the bottom is a concise way of displaying this surface profile using the same shading. In Secs. VI and VII, we use this representation of the surface topography to visualize the time evolution of the surface by placing the stripes corresponding to successive surface profiles under each other.

III. DYNAMIC PROPERTIES FROM SURFACE ANGLE MEASUREMENTS

The phenomenology of wet granular materials is much richer than that of dry samples. The attractive forces between the particles lead to correlated motion of the grains and qualitatively new avalanche dynamics. These new types of avalanches form rough and highly variable surfaces. In order to capture the most fundamental features of our system, however, we will initially neglect these surface features and examine only the *overall surface angle* [Fig. 2(e)] to describe the observed surfaces with a single number. This approach allows us to compare our results directly to the behavior of dry materials, where the surface is virtually flat and is completely described by its inclination angle.

Figure 3 shows the time evolution of the surface angle for various rotation rates. As in the case of dry materials we observe discrete avalanches at low rotation rates. We find that $\theta(t)$ in this regime is a typical sawtooth-shaped function looking very similar to the force-displacement curve of stick-slip processes, which is not very surprising since stick-slip-like behavior is quite common in granular materials [25–28]. The local maximum and minimum points of $\theta(t)$ correspond to the maximum angle of stability ($\theta_{\max}$) and the repose angle θ_r, respectively. Note that if we plot the surface angle as a function of the rotation angle of the drum (the angle that a given direction in the rotation plane of the drum makes with the horizontal), the increasing segments of the curve are straight lines with a slope of unity. If we gradually increase the angular velocity of the drum, then at a given rotation rate ($\Omega = 4$ rpm in Fig. 3) the flow becomes continuous, and after some transients the surface angle becomes constant. In this section, we consider the avalanching regime (at $\Omega = 0.12$ rpm, except where noted otherwise) and investigate how the characteristic angles and the avalanche size distribution depend on the liquid content and the rotation rate. The transition to continuous flows is described in the following section.

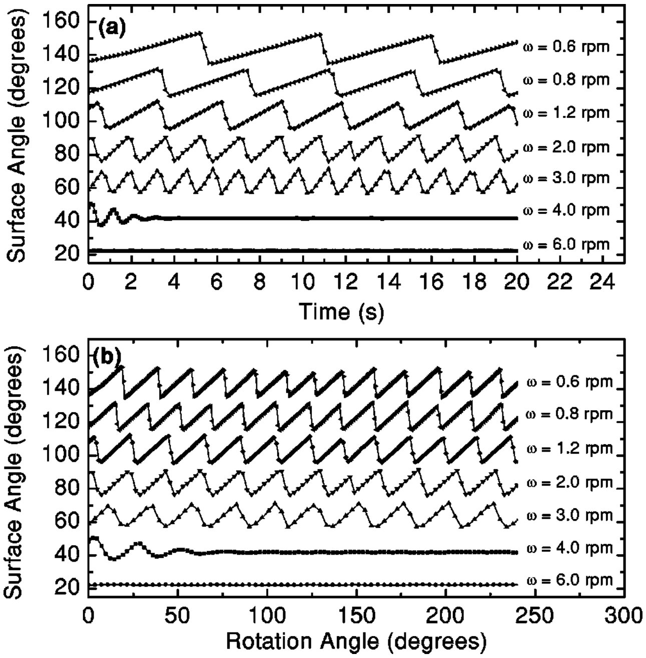

FIG. 3. The temporal variation of the surface angle at various rotation rates (a) as a function of time and (b) as a function of the rotation angle of the drum. These data were taken using the large $d = 0.9$ mm beads, and the liquid content was $\tau = 0.009\%$. Note that the curves are shifted by increments of 20° for clarity.

A. The maximum and the repose angle

Figure 4 shows the maximum angle just before an avalanche, $\langle\theta_{\max}\rangle$, and the angle of repose after an avalanche, $\langle\theta_r\rangle$, as a function of liquid content for the three different bead sizes (averaged over several hundred avalanches). The measured angles have distributions of finite width, the error bars in the figure indicate their standard deviation. These characteristic angles reveal essential properties of the material: $\theta_{\max}$ reflects the stability of the sample while θ_r is also related to the dissipation during the avalanche events. The various features of these curves reflect changes in the dynamic behavior corresponding to the three regimes mentioned in the Introduction, which are described in this section through qualitative observations, and are more quantitatively characterized in Sec. VI.

The curves corresponding to the smaller bead sizes $d = 0.5$ mm [Fig. 4(b)] and $d = 0.35$ mm [Fig. 4(c)] are quite similar. At the lowest liquid contents, very small avalanches are observed. This is the granular regime, where the behavior is qualitatively similar to that of dry granular materials. Due to the interparticle cohesive forces, $\theta_{\max}$ in this regime is slightly larger than the value measured in dry samples. On the other hand, θ_r hardly changes, presumably because the presence of interstitial liquid does not significantly alter the dissipation in the fluidized layer of rolling beads.

At higher liquid contents, in the correlated regime, the increased cohesive force results in a larger increase in $\theta_{\max}$.

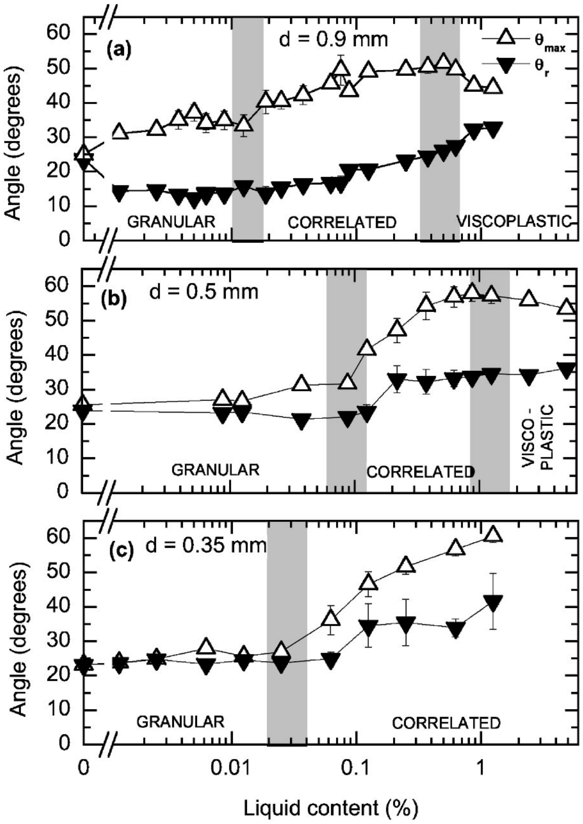

FIG. 4. The dependence of the maximum angle $\theta_{\max}$ and the repose angle θ_r on the liquid content for three different bead sizes. (a) $d=0.9$ mm, $\Omega=0.12$ rpm, (b) $d=0.5$ mm, $\Omega=0.12$ rpm, (c) $d=0.35$ mm, $\Omega=0.03$ rpm (a lower rotation rate was chosen because at $\Omega=0.12$ rpm the smallest beads exhibit continuous flow for the lowest liquid contents). Gray stripes indicate the approximate boundaries of the regimes.

In this regime, the beads on the top surface are more effectively stabilized by the cohesive forces, thus failure leading to an avalanche occurs in the bulk of the sample, and the avalanche flow includes the motion of correlated clumps. We find that θ_r also displays a sudden increase, but at somewhat higher liquid contents than the increase in $\theta_{\max}$. This offset is possibly due to the motion of the clump fluidizing the underlying layer of beads, thus individual rolling grains help determine the final slope as in the granular regime. At higher liquid contents, the cohesive and viscous forces would prevent such fluidization leading to the increase in θ_r.

At the highest liquid contents, $\theta_{\max}$ slightly decreases in Figs. 4(a) and 4(b). This decrease in the stability of the material, also observed in our previous studies of the repose angle using a different technique [12], is probably related to lubrication effects decreasing the static friction among the grains. In this regime, the nature of the avalanches changes again: the material is transported by coherent flow extending over the whole surface of the sample. We did not observe this regime for the $d=0.35$ mm beads, possibly because the cohesive forces are much stronger relative to the weight of those beads. A careful examination of Fig. 4 reveals a few other differences between the different grains studied such as the relatively large avalanches exhibited by the $d=0.9$ mm beads even at very low liquid contents. These differences are difficult to interpret, since we only examined three grain samples that varied not only in their size, but presumably also in their microscopic surface properties. For the same reasons, our data do not enable us to introduce simple dimensionless quantities that could eliminate bead size from the parameters.

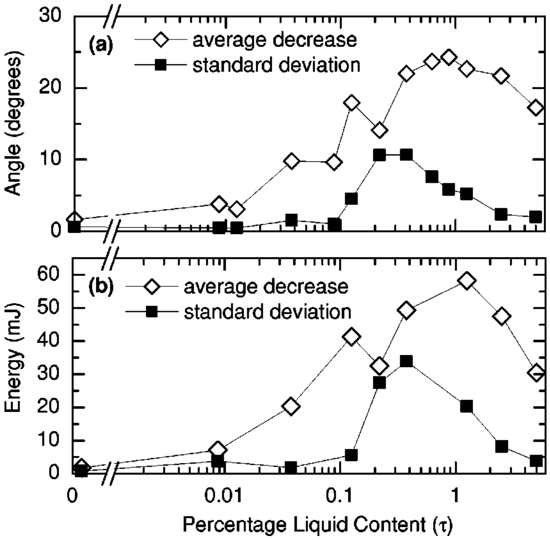

FIG. 5. The average avalanche size and the width of the avalanche size distribution as a function of liquid content, calculated with two different methods. (a) Decrease in the surface angle, $\langle\Delta\theta\rangle$, $2\sigma(\Delta\theta)$ and (b) decrease in the potential energy, $\langle\Delta E\rangle$, $2\sigma(\Delta E)$. The data were taken using medium sized beads, $d=0.5$ mm, $\Omega=0.12$ rpm.

B. Statistics of avalanche sizes

So far, we have restricted our discussion to the average values $\langle\theta_{\max}\rangle$ and $\langle\theta_r\rangle$. The characteristic angles are influenced, however, by the microstructure of the sample, i.e., the actual configuration of the grains, which leads to inherent fluctuations and a nontrivial distribution of the measured quantities. The analysis of these distributions may provide insight into the internal dynamics of the material. In particular, the statistics of avalanche sizes has attracted much recent attention due to its possible connection to self-organized criticality [16,18–20,23,29–31].

In this section, we analyze the statistical distribution of avalanche sizes. The simplest quantity that describes the size of an avalanche is $\Delta\theta=\theta_{\max}-\theta_r$, which has been widely used to characterize avalanches among dry grains in a rotating drum [19,32]. In Fig. 5(a), we plot the average avalanche size

$$\langle\Delta\theta\rangle=\frac{1}{N}\sum_{i=1}^{N}\Delta\theta_i \tag{1}$$

(where $\Delta\theta_i$, $i=1,\ldots,N$ is the angle drop in the ith avalanche) and the width of the avalanche size distribution

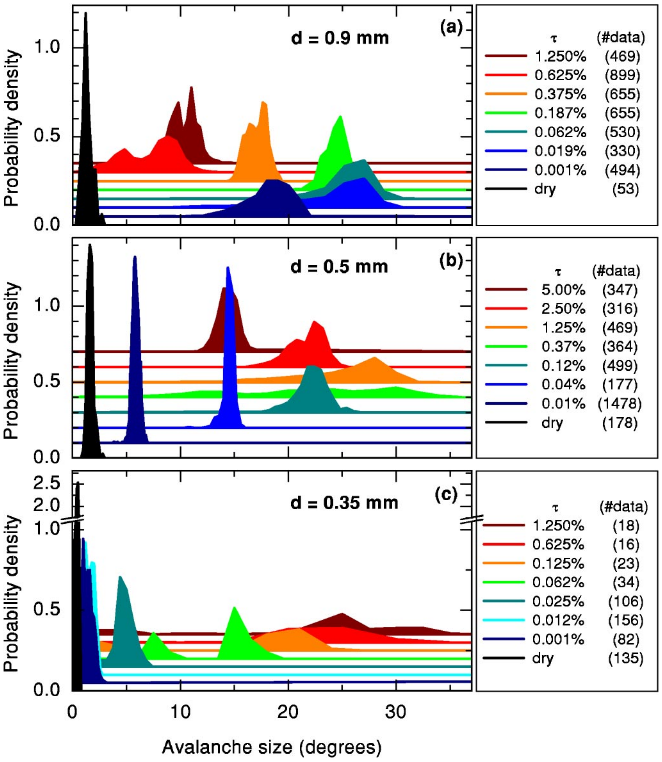

FIG. 6. (Color online) Distribution of the avalanche size ($\Delta\theta$) for various liquid contents. (a) Large beads, $d=0.9$ mm, $\Omega=0.12$ rpm; (b) medium beads, $d=0.5$ mm, $\Omega=0.12$ rpm; (c) small beads, $d=0.35$ mm, $\Omega=0.03$ rpm. The right-hand column shows the number of avalanches included for each sample—note that the statistics are much better for the large and medium beads than for the smaller beads.

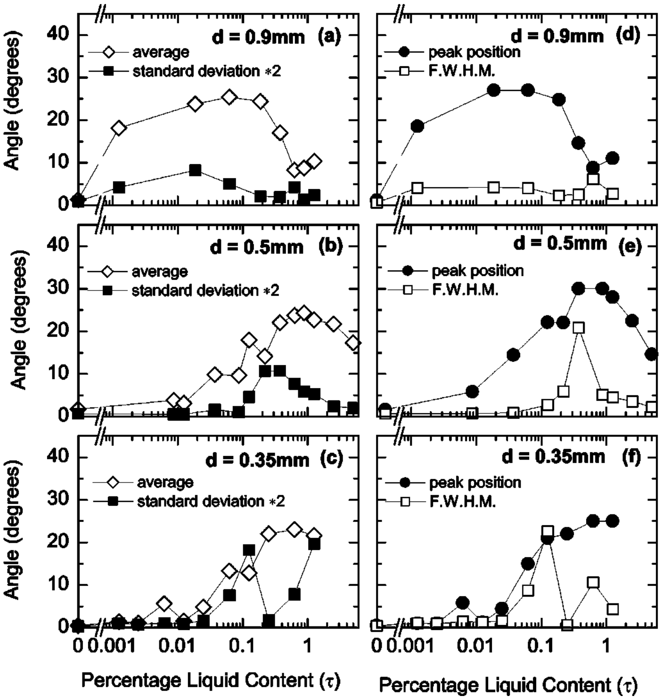

FIG. 7. Statistical measures of the avalanche size distributions presented in Fig. 6 for the three different bead sizes as indicated in the figure. (a)–(c) The average angle drop: $\langle\Delta\theta\rangle$ and the standard deviation $2\sigma(\Delta\theta)$ (see text). (d)–(f) The most probable avalanche size, i.e., the maximum of $P(\Delta\theta)$ (peak position), and the full width at half maximum (FWHM) of the peaks.

$$\sigma(\Delta\theta)=\sqrt{\frac{N\sum_{i=1}^{N}\Delta\theta_i^2-\left(\sum_{i=1}^{N}\Delta\theta\right)^2}{N(N-1)}} \tag{2}$$

for the $d=0.5$ mm beads. (Note that we do not assume that the distribution is Gaussian, we just use the standard deviation as a measure of the width of the distribution.) Since the definition of the surface angle is somewhat arbitrary in the case of our surfaces that can be both rough and have global curvature (as discussed below), we also define an alternative measure of the avalanche size, $\Delta E=mg(h_1-h_2)$, where m is the mass of the sample, g is the gravitational acceleration, h_1 and h_2 are the vertical positions of the center of mass of the sample before and after the avalanche, respectively. The energy difference ΔE is simply the difference between the potential energies of the sample just before and just after an avalanche [33]. The analogous quantities $\langle\Delta E\rangle$ and $2\sigma(\Delta E)$ are plotted in Fig. 5(b). The graphs indicate that the two different measures of the avalanche size yield almost equivalent results, thus we use the standard $\Delta\theta$ as the measure of the avalanche size in the following discussion. In order to characterize the distribution in more detail, in Fig. 6 we plot the measured probability densities $P(\Delta\theta)$ for several liquid contents for the three different bead sizes, where $P(\Delta\theta)d\theta$ is the probability for the avalanche size to fall between $\Delta\theta$ and $\Delta\theta+d\theta$ [we estimate $P(\Delta\theta)$ from histograms]. In Fig. 7, we also plot several statistical measures characterizing these distributions including the peak position [the maximum of $P(\Delta\theta)$] and the FWHM (full width of the peak at half of the maximum value).

The statistical properties of the avalanches shown in Figs. 6 and 7 exhibit several interesting features. The size of the typical avalanche quickly increases with increasing liquid content reflecting the increasing cohesion, then a decrease is observed when the viscoplastic regime is reached. At the lowest liquid contents, we observe single peaks, i.e., the system has a characteristic avalanche size with noiselike variations. At larger liquid contents, however, in several cases we observe double peaks or extremely broad avalanche size distributions. This implies the existence of two or more characteristic avalanche sizes, i.e., both small and large avalanches may occur. A similar feature has been observed in fine cohesive powders [23]. As discussed below, this phenomenon is related to the fact that at high liquid contents, the surface is far from being flat and both the limit of stability and the size of the avalanche depend strongly on the shape of the actual surface.

Within a rotating drum experiment, the initial condition for an avalanche is the surface profile formed by the previous avalanche. The shapes of the surfaces after successive avalanches can thus be regarded as steps of a special dynamical map. In the granular regime, the freely rolling grains always smooth out the surface, so this mapping is trivial. However, in the correlated regime, where the existence of clumps leads

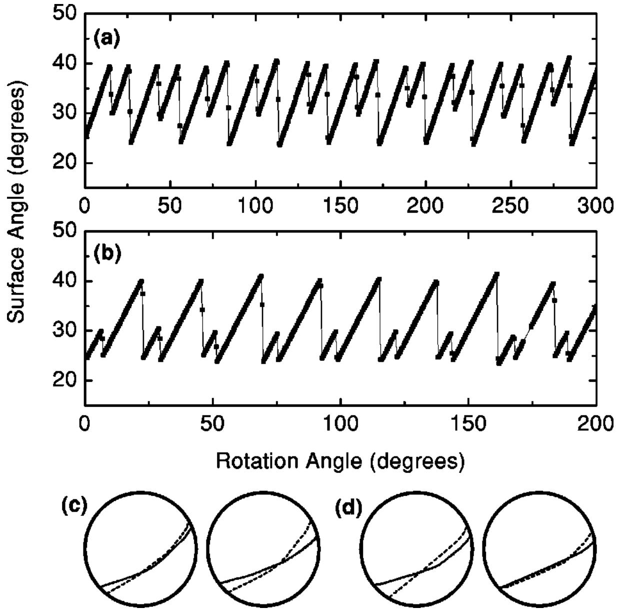

FIG. 8. Alternating small and large avalanches. (a) $d=0.5$ mm, $\tau=0.125\%$, $\Omega=0.4$ rpm, (b) $d=0.35$ mm, $\tau=0.062\%$, $\Omega=0.15$ rpm. (c) and (d) The initial (dashed line) and final (solid line) surface profiles for two successive avalanches. The parameters are the same as in (a) and (b), respectively. Unfortunately, due to the fluctuations in the system, these patterns of behavior were difficult to create reproducibly.

to rugged surfaces, this map is rather complex. Due to the inherent fluctuations in the system, in most cases this mapping is stochastic, smaller and larger avalanches follow each other in a largely random manner. In some cases, however, the system reaches quasistable fixed points (when all the avalanches are very similar and their initial and final surfaces are rotated versions of each other), or limit cycles, when the initial profile is recovered in two or more avalanches. Two examples for this latter case are shown in Fig. 8. Unfortunately, the fluctuations in our system usually destroy regular behavior, and thus we could not perform a detailed investigation of this map. However, we expect that a corresponding model system without strong fluctuations would display an extremely rich chaotic behavior.

C. Logarithmic aging

As expected from previous studies, and shown in Sec. III A, $\theta_{\max}$ strongly depends on the liquid content due to the increasing capillary forces. Our measurements indicate that $\theta_{\max}$ also depends on the rotation rate Ω. Although (for small Ω) the rotation rate only influences the waiting time between successive avalanches, $\theta_{\max}$ clearly decreases with increasing rotation rate. This effect (which is also visible in the measurements of the surface as a function of drum rotation rate shown below) is presented in Figs. 9(a) and 9(b), which show $\theta_{\max}$ as a function of the waiting time, i.e., the time between avalanche events which decreases with increasing

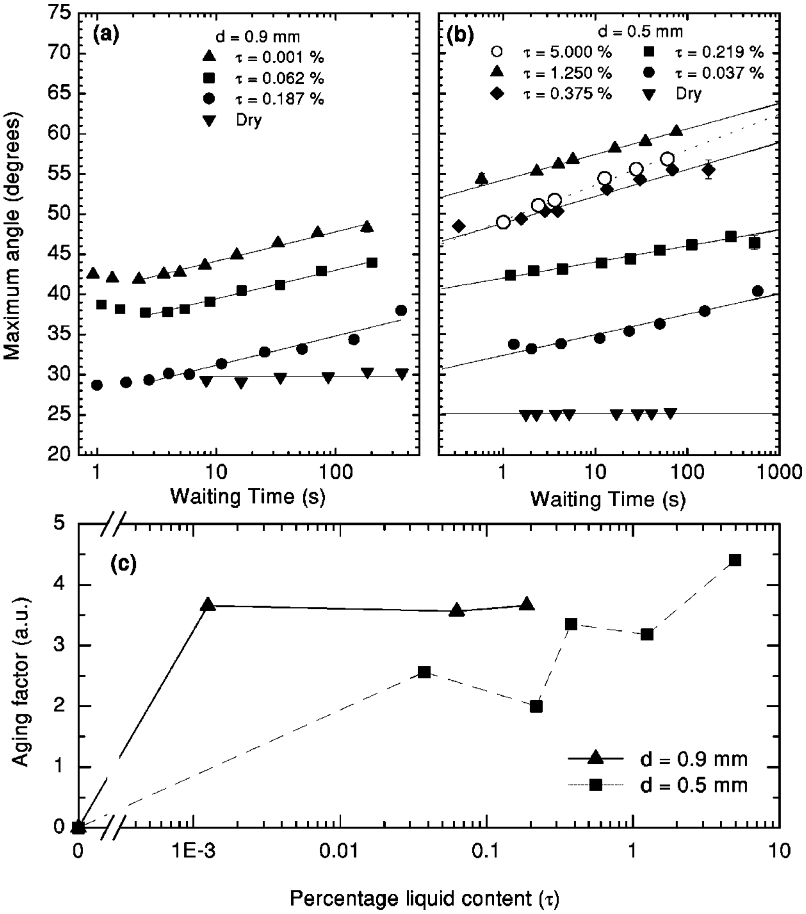

FIG. 9. (a),(b) The dependence of the maximum angle $\theta_{\max}$ on the average waiting time between successive avalanches. The system exhibits aging: longer waiting times between avalanches leads to increased stability. The continuous lines are logarithmic fits to the data. (a) $d=0.9$ mm, (b) $d=0.5$ mm. (c) The intensity of aging [i.e., the slope of the fitted straight lines in (a) and (b)] as a function of liquid content for the two different bead sizes.

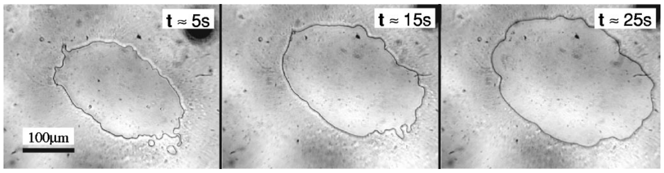

FIG. 10. The oil at the contact point of a wet bead (similar to the ones used in the experiment, but $d=1.2$ mm) and the glass plate on which it rests. The images are taken from above at different time instants via phase-contrast microscopy. The delay time from the instant when the bead was placed on the plate was (a) $t\approx 5$ sec, (b) $t\approx 15$ sec, (c) $t\approx 25$ sec. The flow of oil to the contact point thus occurs on a time scale of several seconds, suggesting a natural explanation for our observed aging effects.

rotation rate. The curves indicate a logarithmic increase in the stability of the system. In Fig. 9(c), we also present the intensity of the aging process (quantified as the slope of the fitted straight lines). We do not observe aging for the dry samples, and the effect is somewhat stronger for the larger liquid contents, though on the basis of our data we cannot determine the exact functional form.

Similar aging effects have been observed in several different granular experiments [8,34], but the underlying mechanisms are complex, since several factors may play an important role [34]. Since in our experiment the effect is more pronounced at higher liquid contents, and the vapor pressure of oil is low, we attribute it to the motion of oil flowing towards the contact points rather than condensation effects [8]. This assumption is also supported by our investigations of a wet contact by phase-contrast microscopy. We placed a wet bead on the object plate and observed a flow of oil to the region of the contact point (Fig. 10). Our observations revealed that a liquid bridge is formed when the bead was placed on the plate, and the bridge's shape continues to change slowly even after several seconds of waiting time. This finding further supports the importance of viscosity in addition to the surface tension as an important parameter in understanding the behavior of wet granular media, as was previously demonstrated by Samadani and Kudrolli [10,11].

IV. THE ROLE OF THE ROTATION RATE: AVALANCHES AND CONTINUOUS FLOW

A. Hysteresis in the transition between continuous and avalanching flows

As mentioned above, if the rotation rate is increased above a threshold, the system exhibits continuous flow instead of discrete avalanches. Earlier studies in dry media revealed that the transition between avalanching and continuous flows is hysteretic in rotation rate [19,35]. Now we have investigated the avalanching-continuous flow transition for various liquid contents. We slowly increased and then decreased the rotation rate and measured the average surface angle in the continuous regime as well as $\theta_{\max}$ and θ_r in the avalanching regime. The rotation rate was changed in discrete steps by factors between 1.2 and 1.4, each step was performed with a constant angular acceleration in 3 s. Between the steps, the drum was rotated for typically 0.5–1 full rotation to determine whether the flow is continuous or avalanching (the minimum rotation was 90° at some of the lowest rotation rates, the maximum was 40 full rotations at $\Omega=30$ rpm). We consider the flow continuous when the medium never comes to rest with respect to the drum, which coincides with $\Delta\theta\equiv\theta_{\max}-\theta_r<1°$. The results of typical runs are presented in Figs. 11(a)–11(c), where $\theta_{\max}$ and θ_r are plotted as a function of the rotation rate.

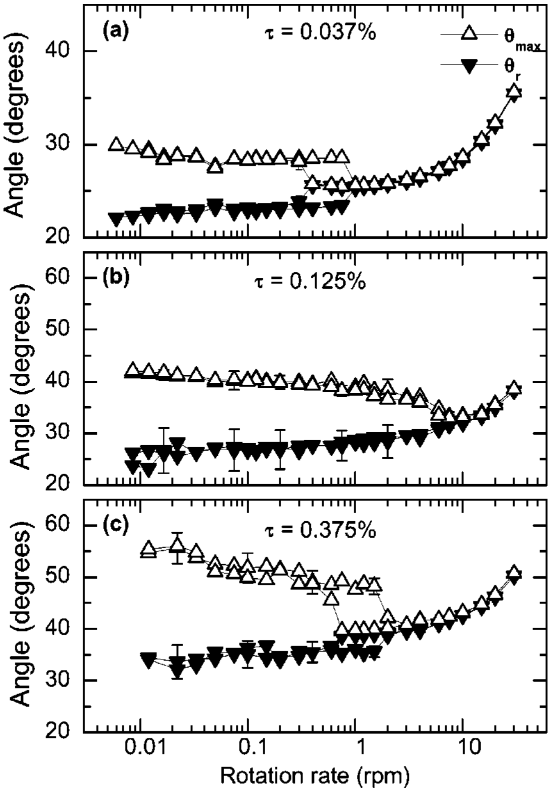

FIG. 11. (a)–(c) $\theta_{\max}$ and θ_r as a function of rotation rate for three different liquid contents, $d=0.5$ mm. The error bars represent the standard deviation of the observed angle distributions.

The three basic regimes of behavior observed previously are also reflected in the nature of the transition. In the granular regime at low liquid contents (e.g., $\tau=0.037\%$), where the behavior is qualitatively similar to the dry case, we observe a clear hysteretic transition between continuous and avalanching flow [Fig. 11(a)]. At a somewhat higher liquid content, [$\tau=0.125\%$, see Fig. 11(b)] the correlated behavior is marked by a lack of hysteresis, and intermittent avalanches are observed at a relatively high rotation rate compared to the other regimes. The continuous flow in this regime consists of a stream of separated clumps rather than the constant flux seen in the other two regimes. At $\tau=0.375\%$ [Fig. 11(c)], hysteresis is again observed, coinciding with the onset of the viscoplastic continuous flow, which is smooth and coherent over the entire sample.

The origin of the hysteresis in the transition between continuous and avalanching flows is an interesting subject [19,35–37], but a detailed discussion goes beyond the scope of this paper. We hypothesize that the hysteresis is observed because the transitions on increasing and decreasing the rotation rate have different origins, thus they do not necessarily coincide. A rough explanation of the transition from avalanching flow to continuous flow is that the successive avalanches merge. More precisely, at high velocities the rotation during the avalanche is becoming important and the constant energy supply prevents the grains from stopping. For the reverse transition, the continuous flow cannot be maintained at arbitrarily low velocities because then the flowing layer cannot stay fluidized, and the grains get stuck in small depressions of the underlying layer.

The nature of the transition is naturally different in different wetting regimes. In the granular and the viscoplastic regimes, the constant material flux in the continuous flow phase is qualitatively different from the first increasing and then decreasing flux observed in the case of an avalanche. Thus, the intermittent and the continuous flow may represent two locally stable dynamical phases with a hysteretic transition between them. On the other hand, in the correlated regime there is no qualitative change in the flow dynamics when the motion becomes continuous: the successive clumps do not merge even if their motion overlaps in time. According to the arguments advanced by Rajchenbach [19], the characteristic fall time of the grains is thus the same in the avalanching and the continuous flow, and we observe no hysteresis.

B. The phase diagram

We summarize our measurements of the different flow regimes in a phase diagram (Fig. 12) indicating the nature of the flow as a function of liquid content and rotation rate. Each symbol corresponds to a measurement, gray symbols denote avalanches, black symbols denote continuous flow, and white symbols mark the hysteretic regions. For the largest beads with $d=0.9$ mm [Fig. 12(a)], the three regimes are clearly visible. Near $\tau\approx 0.02\%$, the disappearance of hysteresis and the displacement of the transition point toward higher rotation rates indicate the transition from the granular to the correlated regime. The sudden change in the transition point around $\tau\approx 0.1\%$ marks the onset of the viscoplastic continuous flow.

We have fewer data points for medium ($d=0.5$ mm) and small ($d=0.35$ mm) beads, respectively, but the main trends are visible [Figs. 12(b) and 12(c)]. A universal feature of the phase diagrams is that, upon approaching the correlated regime from the granular regime, the transition point moves towards higher rotation rates. This suggests that the clump formation leads to more effective transport and quicker avalanches as was noted in our previous draining crater studies [12]. A general trend is that for smaller beads the transition to correlated behavior occurs at higher liquid contents, most probably due to the larger internal surface of these samples.

The most striking feature is that as the bead size is decreased, the viscoplastic behavior and, in particular, the region of the viscoplastic continuous flow diminishes. For the $d=0.5$ mm beads, it is restricted to the region between $0.3\%\lesssim\tau\lesssim 0.8\%$ and $1\text{ rpm}\lesssim\Omega\lesssim 10$ rpm, and the $d=0.35$ mm beads exhibit no viscoplastic flow at all. A possible explanation is that in samples consisting of smaller beads, the number of contacts at the boundary of a given volume of material is much larger, therefore the cohesive forces dominate inertial effects. For smaller beads, the hysteresis of the continuous-to-avalanche transition also seems to decrease, but this is difficult to interpret and will require further investigation to understand.

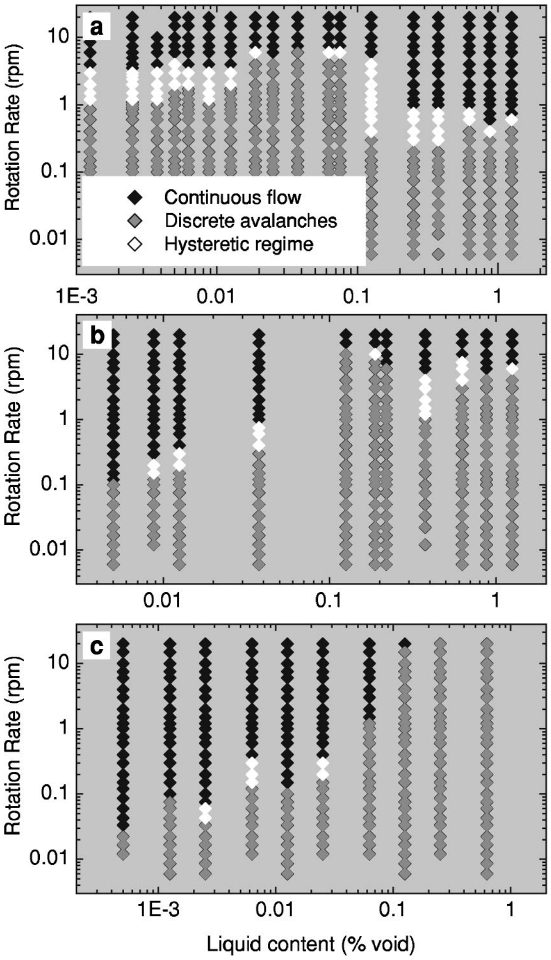

FIG. 12. (a) Phase diagram of the dynamic behavior as a function of the liquid content τ and the rotation rate Ω. (a) Large beads, $d=0.9$ mm, (b) medium beads, $d=0.5$ mm, (c) small beads, $d=0.35$ mm.

We have performed some preliminary measurements on the role of the viscosity of the interstitial liquid (not shown here). Experiments with a highly viscous silicon oil yielded viscoplastic flow in a wider range of liquid contents and rotation rates. These results are again consistent with the findings of Samandani and Kudrolli [11] that viscosity plays an important role in these processes.

V. SURFACE MORPHOLOGY

Up to this point we have described the surface by a single quantity, the overall surface angle, but the actual surfaces are rough and have significant curvature. This morphology contains additional information about the system, and should be useful in producing realistic models of wet granular flow. Figure 13 shows sample surface profiles for various materials. The graph confirms that the wet samples form exotic surfaces, especially for the smaller beads. Note that besides

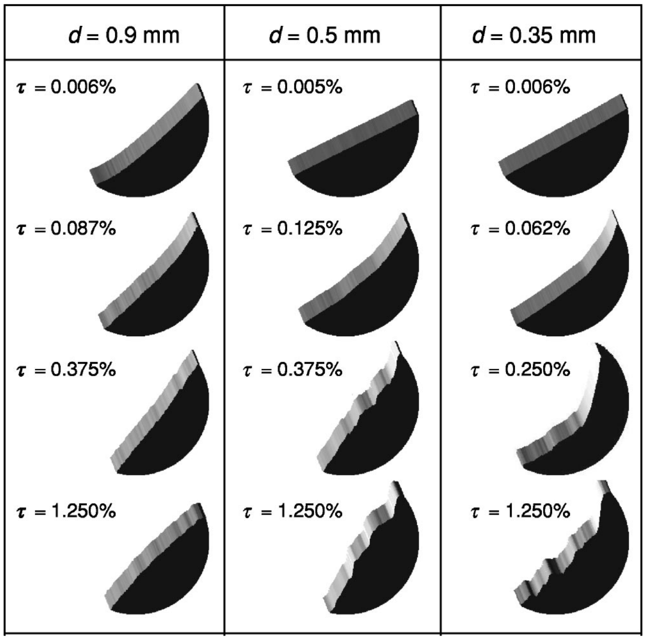

FIG. 13. Sample surfaces for various materials, as indicated in the figure. The images were taken right before an avalanche, the rotation rate was $\Omega = 0.05$ rpm for the large and medium beads and $\Omega = 0.043$ rpm for the small beads. Note that the surface is close to flat in the granular regime, mostly concave in the correlated regime and mostly convex in the viscoplastic regime. Note also the smaller scale structure at the smaller bead sizes.

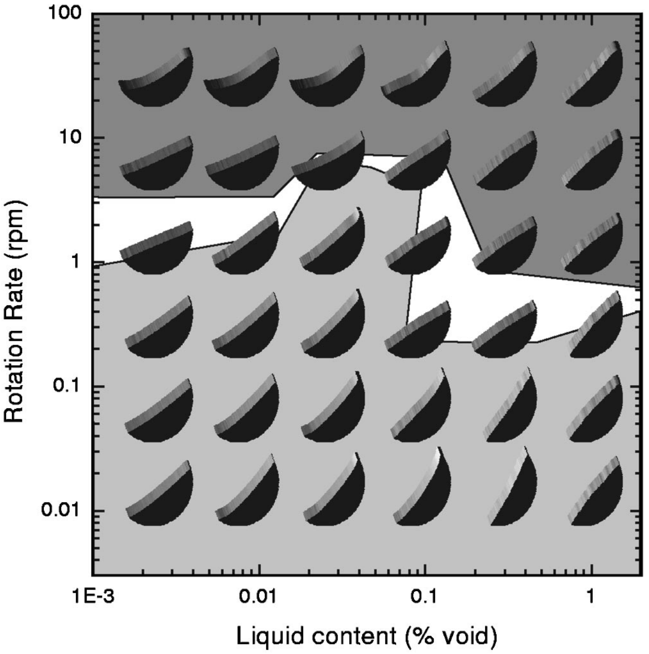

FIG. 14. Shape of the surface at various points of the parameter space for the large $d = 0.9$ mm beads. A sketch of the phase diagram is shown in gray scale in the background: the dark gray region denotes continuous flow, the light gray region corresponds to avalanches; the white area is the hysteretic regime. The shape changes both as a function of Ω and τ. At the highest rotation rates the S-shaped regime [19] is clearly observable.

the overall shape of the surface, some smaller scale roughness is also observable for the larger liquid contents. These small scale features typically are random and fluctuate between avalanches. In the viscoplastic regime, however, the coherence of the flow strongly reduces fluctuations, and a robust pattern is formed which is reproduced at the end of each avalanche (as discussed in Sec. VI B below).

Since the surfaces of the largest ($d = 0.9$ mm) bead samples are relatively simple, we investigate them in more detail. Figure 14 shows sample surfaces for the $d = 0.9$ mm beads at various liquid contents and rotation rates. In the granular regime, the surface is almost flat, correlated avalanches typically form concave surfaces, and the viscoplastic flow typically results in a convex surface. Furthermore, at the highest rotation rates, the surface is S shaped due to inertial effects across the entire wetness range [19]. The convexity of the surface can be characterized quantitatively several ways [38]. A simple and robust measure is the integrated area κ between the surface profile $[h(x)]$ and the straight line connecting the two ends of the surface line. For a flat surface where $h(x)$ is a straight line, $\kappa = 0$; $\kappa < 0$ implies a predominantly concave surface, $\kappa > 0$ implies a predominantly convex surface.

In Fig. 15, the value of κ is indicated by the color of symbols as a function of τ and Ω. Black symbols correspond to concave surfaces (negative κ), and approximately indicate the correlated regime. White symbols are used for positive κ values, corresponding to the viscoplastic regime. Gray symbols indicate that $\kappa \approx 0$, either because the surface is flat (upper left region of Fig. 15—this is approximately the granular regime) or because convex and concave parts are balanced (at the boundary of correlated and viscoplastic regimes). For comparison, we also show the typical observed surface shapes for the medium sized ($d = 0.5$ mm) beads (Fig. 16). Also, here the convexity of the surface seems to correlate with the different flow regimes, however, some additional smaller scale features are also observable.

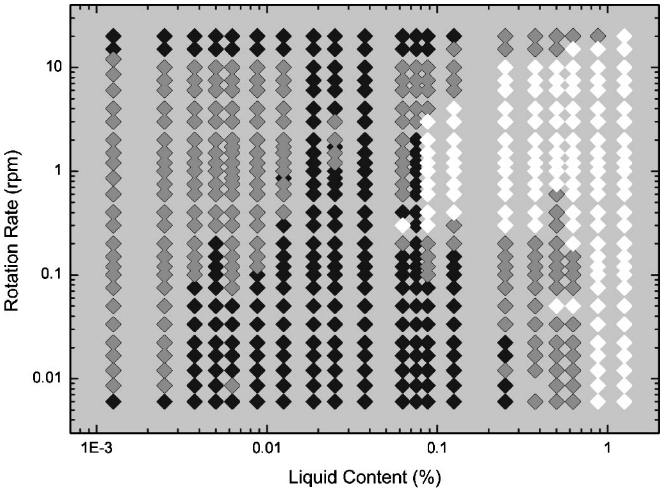

FIG. 15. The value of convexity parameter κ as a function of the rotation rate and the liquid content for the large beads, $d = 0.9$ mm. Black symbols, concave surface ($\kappa < 0$), white symbols, convex surface ($\kappa > 0$), gray symbols, ($\kappa \approx 0$).

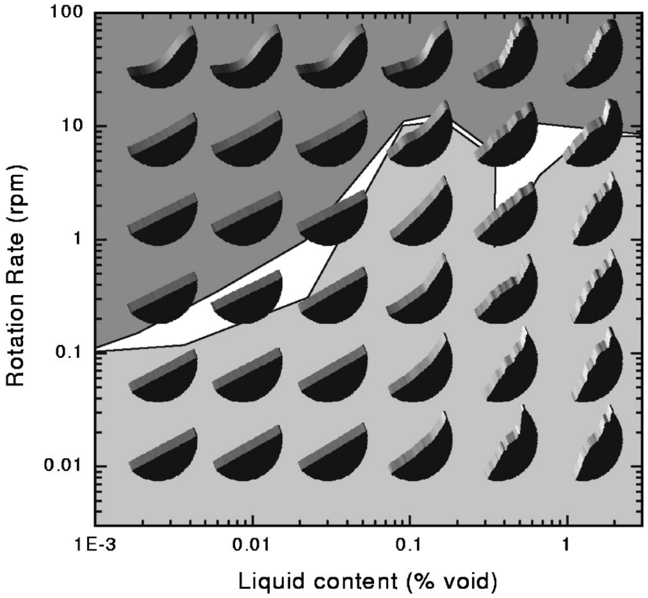

FIG. 16. Shape of the surface at various points of the parameter space for the medium $d=0.5$ mm beads (see the caption of Fig. 14 for further explanation). The observed surface shapes are more complicated for these beads compared to the $d=0.9$ mm beads, but the overall convex vs concave nature is similar.

Clearly, the phase boundaries in Fig. 15 are not vertical lines. This means that the liquid content is not the only parameter influencing the behavior: changing the rotation rate can also switch between different flow mechanisms. This observation implies that the formation of correlated clumps is a dynamic process with characteristic times comparable to the other time scales of the experiment. We expect that the different convexity in the different regimes could be reproduced relatively easily in the framework of a continuum model. A detailed explanation of the surface shapes, however, would probably require a full analysis of the avalanche dynamics.

VI. DETAILED DYNAMICS OF AVALANCHES

The rotating drum apparatus allows us to obtain information not just about the medium before and after the avalanche events, but also about the details of the grain motion *during avalanche events*. In order to analyze the dynamics of avalanches, we have obtained two-dimensional space-time matrices $h(x,t)$ characterizing the sample surfaces throughout the avalanche process. These matrices can then be analyzed to produce a variety of information about the individual avalanches. By taking derivatives of the $h(x,t)$ data, we obtain the local angle $\alpha(x,t)=\arctan[\partial_x h(x,t)]$ and the local vertical velocity $u(x,t)=\partial_t h(x,t)$ of the surface profile. Furthermore, by integrating the vertical velocity (using the continuity equation and assuming constant density [39]), we also obtain the local flux in the avalanche, i.e., $\phi(x,t)=\rho w\int_{-D/2}^{x}\partial_t h(x',t)dx'$ (where ρ is the grain density, w is the width of the drum, and D is the drum diameter), which represents the material flowing through a given vertical plane at position x. In Fig. 17(a), we present snapshots of the progression of single avalanches for several typical liquid contents. Figure 17(b) displays $\alpha(x,t)$ as a function of space (horizontally) and time (downwards) for the same individual avalanches. In Figs. 17(c)–17(e), we present the average behavior of 300–500 avalanches at the same liquid contents, and show similar graphs of the time evolution of $\langle\alpha(x,t)\rangle$, $\langle u(x,t)\rangle$, and $\langle\phi(x,t)\rangle$, where $\langle\ \rangle$ denotes averaging over avalanches. By obtaining these quantitative measures of the averaged properties, we can separate the robust characteristics of the avalanche dynamics from the large fluctuations that are inherent in avalanche processes.

The averaging process raises a few technical questions. First, the order of averaging and numerical differentiation is optional, i.e., we can either calculate $\alpha(x,t)$ and the other quantities from the raw $h(x,t)$ data and perform averaging afterwards or take the averaged $\langle h(x,t)\rangle$ and calculate its numerical derivatives. We verified that the two methods yield equivalent results, and chose the former option.

A second question is how to find the corresponding frames in different recorded avalanches. In order to make this question clear, let us consider the averaging in more detail. Let us assume that we have recorded the variation of the surface profile for N avalanches, and we have N matrices $h_{u,v}^{(i)}$, $i=1,\ldots,N$ denoting the local height in the ith avalanche at position $x=-D/2+u\ \delta x$ and time $t=t_0^{(i)}+v\ \delta t$, where δx and δt are the spatial and temporal resolutions, respectively, and $t_0^{(i)}$ is "the starting time" of the ith avalanche. Then, to obtain the average behavior, we calculate $\langle h_{u,v}\rangle=\Sigma_{i=1}^{N}h_{u,v}^{(i)}/N$. Since the properties of the avalanches (e.g., duration) vary between avalanche events, the appropriate choice for $t_0^{(i)}$ is not trivial. We tried several algorithms and then decided to use the most robust one that was based on the variation of the overall surface angle $\theta(t)$. We fitted straight lines to the segments of the sawtooth signal of $\theta(t)$ (see Fig. 3), and calculated the time $t_{int}^{(i)}$ corresponding to the intersection of the straight lines at the beginning of an avalanche. Then we chose $t_0^{(i)}=t_{int}^{(i)}-0.5$ sec.

A third problem arises from the fact that the $h_{u,v}^{(i)}$ matrices have empty elements: the surfaces do not extend from $-D/2$ to $D/2$. Simply excluding the empty elements from the averaging leads to the appearance of some artifacts at the edges. To resolve this issue, we filled in the empty elements with the value of the closest elements in that row (as if the surface continued horizontally over the edge of the drum), performed the averaging, and then cut down those parts of the averaged profile that were outside the drum. This procedure only influenced the behavior very close to the edges of the sample.

In Fig. 18, we present the same data as a series of curves, where the columns again represent different liquid contents. In the first row of graphs, we plot the averaged surface profiles $\langle h(x)\rangle$ at different time instants during the avalanche. The second row of graphs shows the variation of the local angle $\langle\alpha(x)\rangle$ and the third row plots the local flux $\langle\phi(x)\rangle$ with triangles showing the position of maximum flux. In the following, we analyze the dynamics in the three regimes based on Figs. 17 and 18. We have also magnified parts of Fig. 17 in Fig. 19 to emphasize particular features in the data. For comparison we also show the most important ava-

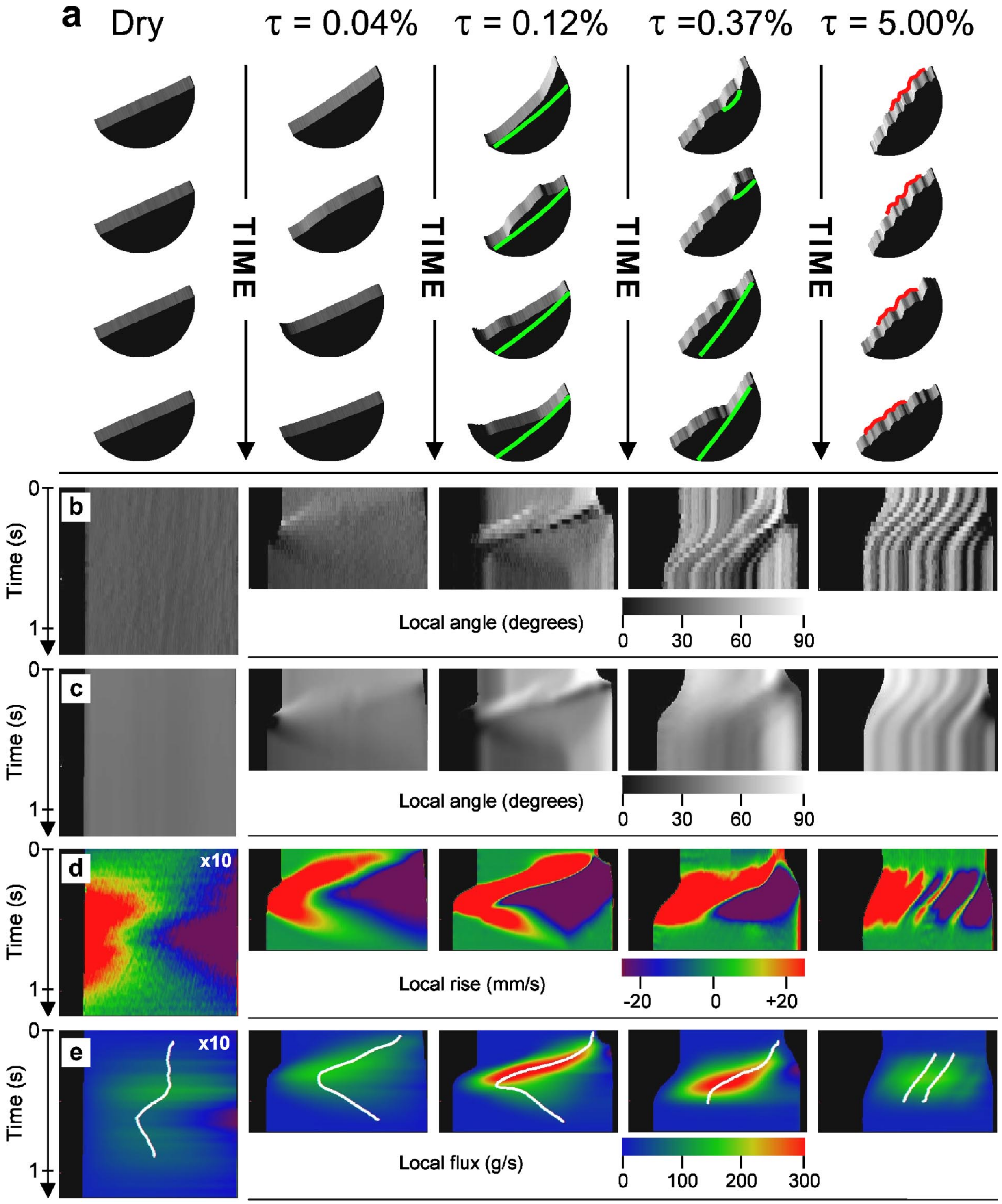

FIG. 17. (Color online) Dynamics of avalanches of different types with grain size $d=0.5$ mm at $\Omega=0.12$ rpm. (a) Snapshots (at 0.1–0.2 sec time intervals) of five single avalanches corresponding to different liquid contents. The third dimension is used for a brightness-coded representation of the local slope α. The colored lines for $\tau=0.12\%$ and 0.37% indicate approximate slip planes in the correlated regime, and the colored lines for $\tau=5.00\%$ show the traveling quasiperiodic surface features in the viscoplastic regime. (b) The local slope with the same brightness coding as a function of space and time. A horizontal line corresponds to a surface profile at a given instant, and time increases downwards (thus avalanches propagate down and to the left). The slanted bright and dark regions correspond to the avalanche front and the kink, respectively (see text). The stripes at higher liquid contents indicate lasting surface features. (c)–(e) The characteristic features of the avalanches averaged over 300–500 avalanche events. The displayed quantities are (c) the local surface angle, (d) the rate of change of local height, and (e) the local grain flux (the white lines indicate the point of maximum current), respectively. Note that the surface patterns at the highest liquid contents are robust against averaging.

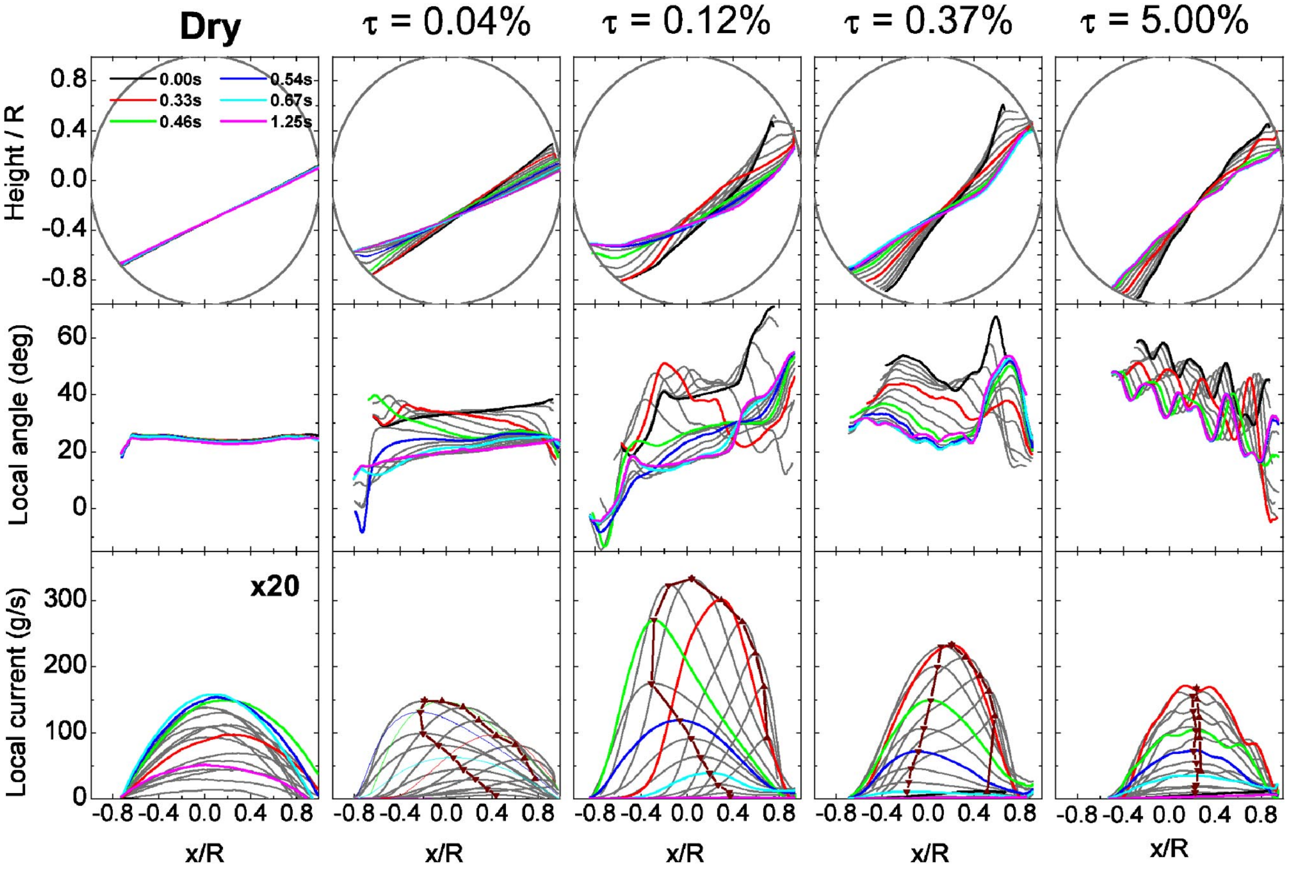

FIG. 18. (Color online) Averaged dynamic parameters: $\langle h(x)\rangle$, $\langle \alpha(x)\rangle$, and $\langle \phi(x)\rangle$ as a function of space at various time instants during the avalanche for five different liquid contents, $d=0.5$ mm, $\Omega=0.12$ rpm. The time interval between successive curves is 0.066 sec, some curves are marked with color as specified in the legend. In the lowest row, triangles mark the point of maximum current. The most important features for different oil contents are the following. Dry samples: The avalanches are very small, and our resolution is insufficient to resolve the detailed dynamics. $\tau=0.04\%$ granular regime: The surface is close to flat, but the local angle is somewhat larger near the top of the slope. The dynamics is dominated by fronts of rolling grains. The region of steeper slope corresponding to the downward propagating front as well as the negative slope of the kink is visible in the graph of the local angle. The point of maximum current also moves downhill then uphill due to the fronts. $\tau=0.12\%$ correlated regime: Failure occurs along a slip plane and a block slides down. The block is best seen in the red curve, the edges are smoothed by the averaging over several hundred avalanches. Some rolling grains are still present, as marked by the presence of the kink. $\tau=0.37\%$ correlated regime: Flow is usually through multiple avalanches, but these are averaged out. The fronts have disappeared, and the angle near the bottom of the slope decreases monotonically. There are lasting contacts during the avalanche, thus the grains cannot roll, and the material stops coherently as a block when it reaches the bottom. $\tau=5.00\%$ viscoplastic regime: The surface moves coherently. The current extends over the whole surface during the whole duration of the avalanche. Curves of the local angle reveal the robust surface patterns as a series of local maxima. During the avalanche, the local maxima move downwards (and spread out slightly), and a new maximum is formed near the top.

lanche types for the $d=0.9$ mm beads in Fig. 20. The qualitative features of the avalanches are quite similar for the two types of beads although the effects are less pronounced for the $d=0.9$ mm beads.

A. The avalanche types

Granular avalanches. With dry grains [15,19,20,30,31,36], the surface remains almost flat throughout the avalanche, and the avalanches have a much longer duration and much smaller flux than in the wet media—as is expected due to the lack of cohesion. Our resolution is not sufficient to distinguish any propagating front in this case, but our system is very similar to that investigated in Ref. [14], all the surface grains are close to the limit of their stability. Thus, we assume that the failure mechanism is similar: the propagation of the front destabilizing the grains is quicker than the material flow. This type of front is marked only by a very slight dilation of the material, which we cannot detect.

With the addition of very small amounts of liquid [e.g., $\tau=0.04\%$, see Fig. 19(a)], the avalanches become much larger due to the onset of intergrain cohesion—this allows us to observe the dynamics in more detail. In this granular regime, the avalanche is always initiated at the top of the surface, and the upper part of the surface is quickly destabilized. As the particles start moving downwards, a front of rolling grains travels downhill. The grains in the lower regions remain at rest until the rolling grains reach them. This type of front corresponds to the ‘‘start down’’ front of Douady *et al.* [40]. The difference in behavior compared to the perfectly

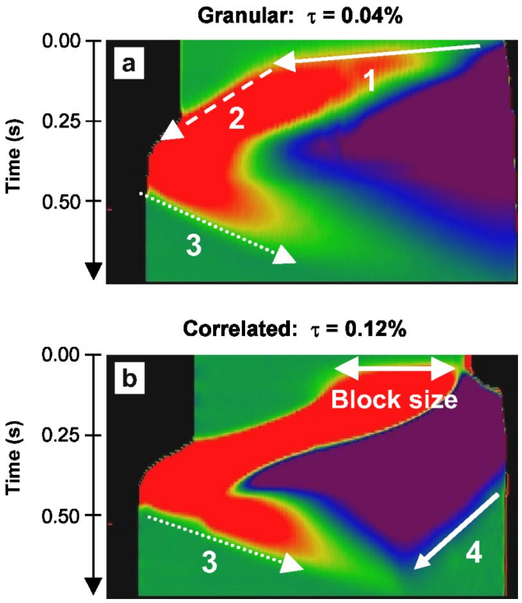

FIG. 19. (Color online) The various fronts observed in our setup in (a) the granular regime ($\tau=0.04\%$) and in (b) the low liquid content region of the correlated regime ($\tau=0.12\%$) for $d=0.5$ mm, $\Omega=0.12$ rpm. The colors indicate the rate of change of local height during the avalanche (see Fig. 17). We observe four different fronts. Front 1: Destabilizing front, this front propagates faster than the material flow via interactions between neighboring grains—destabilizes particles. Front 2: Avalanche front, this front consists of rolling grains, which proceed on a medium at rest and destabilize particles by collisions. Front 3: Kink, the rolling grains accumulate at the lower wall and form a region of low slope there. This slows down the incoming grains, thus this front travels uphill. Front 4: Rear front, the moving grains leave the static ones behind.

dry material can probably be explained by the slight concave curvature of the surface: the grains lower on the slope are in a relatively stable state when the avalanche is initiated.

When the downward-propagating front reaches the wall of the drum at the bottom of the slope, a kind of shockwave is formed, and the rolling of grains is stopped by a region of smaller local angle traveling uphill. This type of front has been classified as a "stop up" front [40], and it corresponds to the "kink" observed in other experiments on dry beads (generally associated with individually rolling grains reaching a solid barrier at the bottom of the slope [41–43]).

Correlated avalanches. At intermediate liquid contents, in the correlated regime $(0.1\%<\tau<2\%)$, the principal failure mechanism is a fracture along a curved slip plane [approximated by the green lines in Fig. 17(a)] analogous to the dynamics of a class of geophysical events known as "slides" [44]. This is the failure mechanism described by the Mohr-Coulomb model [3,6]. At $\tau=0.12\%$ there is a single slip plane, but at larger liquid contents ($\tau=0.37\%$) the avalanches occur through a succession of local slip events. The medium becomes more cohesive with increasing liquid content, preventing grains from moving individually, and thus the kink disappears for $\tau\geqslant0.3\%$ since the material moving as a connected block stops coherently when it hits the bottom.

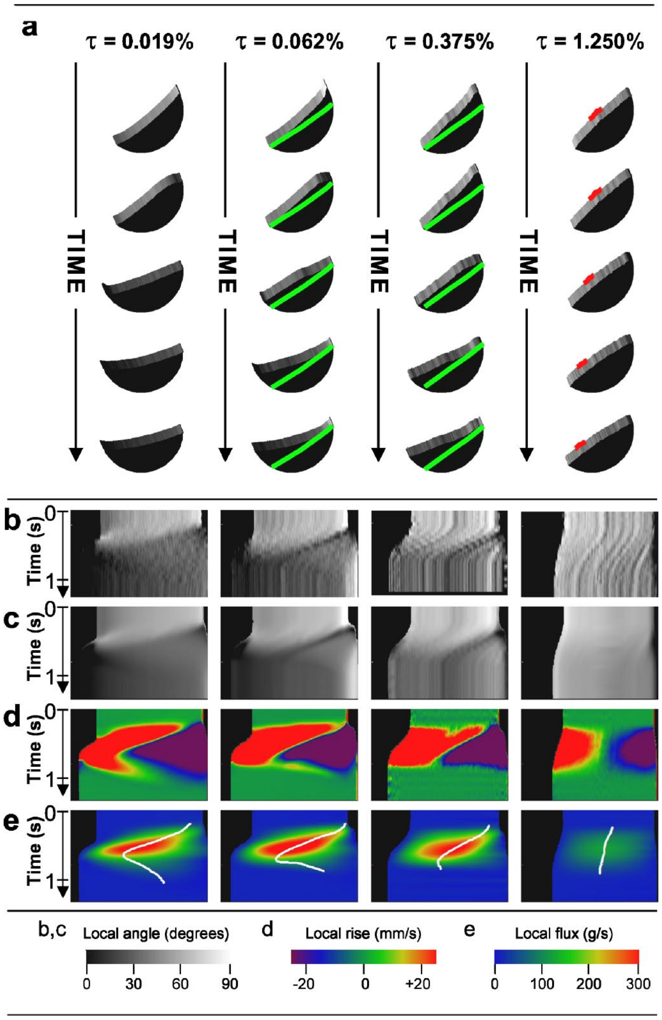

FIG. 20. (Color online) Avalanche dynamics in samples consisting of large beads $d=0.9$ mm. (See also the caption of Fig. 17.)

Viscoplastic avalanches. The onset of the viscoplastic regime ($\tau\approx2\%$) is accompanied by dramatic changes in the behavior. The flow becomes correlated across the entire granular surface as demonstrated by the parallel lines through the avalanche in Fig. 17(b). Since the whole surface moves coherently (rather than breaking apart and evolving separately in different parts of the surface), fluctuations are strongly suppressed [12]. This behavior is qualitatively similar to a different class of geophysical event, called a "debris flow" or "mudflow" [44–46], but the underlying physics may be quite different, since—unlike mudflows—our samples are unsaturated. On the other hand, the decrease in stability due to the increase in liquid content is analogous to the formation of wet snow avalanches [47]. The coherent nature of the motion in this regime leads to such aspects of the dynamics which are not observed in other granular systems, as discussed in the following section.

B. Pattern formation in the viscoplastic regime

One novel property of the viscoplastic avalanches is the robust topology of the top surface that spontaneously forms a nearly periodic pattern [seen in Fig. 17(a)]. This surface structure is maintained essentially intact during the avalanche [note that the lines are continuous throughout the avalanche in Fig. 17(b)], indicating that there are lasting contacts in the flowing layer. Moreover, the pattern is not random, but rather has features that are reproduced at the end of each avalanche. This is demonstrated most clearly in Figs. 18 and in 17(b), where the average of 347 avalanches of the $\tau = 5\%$ sample has the same features as the typical individual avalanche shown in Figs. 17(a) and 17(b). The robust nature of the surface structure of the wettest grains is in sharp contrast to the other regimes where averaging completely smooths out the smaller surface features. We can understand this behavior as resulting from coherence of the entire flow, which strongly reduces fluctuations in this regime. With minimal fluctuations, the final surface structure after each avalanche is essentially the same, thus setting the same initial condition for the next avalanche. With the same initial conditions for each avalanche, naturally the surface features are reproduced each time.

Our experiments with the larger ($d = 0.9$ mm) beads also reveal some pattern formation [see Fig. 20(b)], but with a smaller characteristic size corresponding to 8–10 grain diameters. The difference is probably due to the smaller ratio of the cohesive forces to the gravitational forces on the grains. Due to the small length scale of these patterns, they are largely averaged out, but we have also observed robust patterns that are repeated after each avalanche under several different sets of conditions (see, e.g., Fig. 20, $\tau = 0.375\%$). The dependence of the pattern on grain size and other factors will be the subject of a future investigation.

VII. DYNAMIC PROPERTIES OF CONTINUOUS FLOWS

In the preceding section, we demonstrated that the avalanche dynamics are dramatically different in the three regimes of behavior. The different dynamics are also evident at higher rotation rates where the flow is continuous. In this section, we compare the properties of the continuous flow in the three wetness regimes, with special attention to the viscoplastic flow. Here we only examine the $d = 0.9$ mm beads, since they exhibit viscoplastic continuous flow in the widest range of parameter space.

Figure 21 shows the evolution of the surface profile during different types of continuous flow for $\Omega = 10$ rpm. In the granular regime (e.g., $\tau = 0$ and 0.002%), the surface profile is practically a straight line with only noiselike variations. Our resolution is insufficient to resolve the individually rolling grains in this regime. In contrast, in the correlated regime, the surface is clearly concave, and the flow consists of a succession of clumps moving downhill. From the slope of the stripes in Fig. 21(b), we can estimate the velocity of the moving clumps: $v \approx 50$–60 cm/s. In the viscoplastic regime, the flow is smooth again, and the traveling surface features demonstrate that there are lasting contacts in the flowing layer. The slopes of stripes indicate that the flow is much slower in this regime, $v \approx 10$–15 cm/s. We note that the rotation rate is the same for all the presented liquid contents, meaning that the material flux is constant. The difference in surface velocity thus presumably indicates that the moving layer is much deeper in the case of viscoplastic flow.

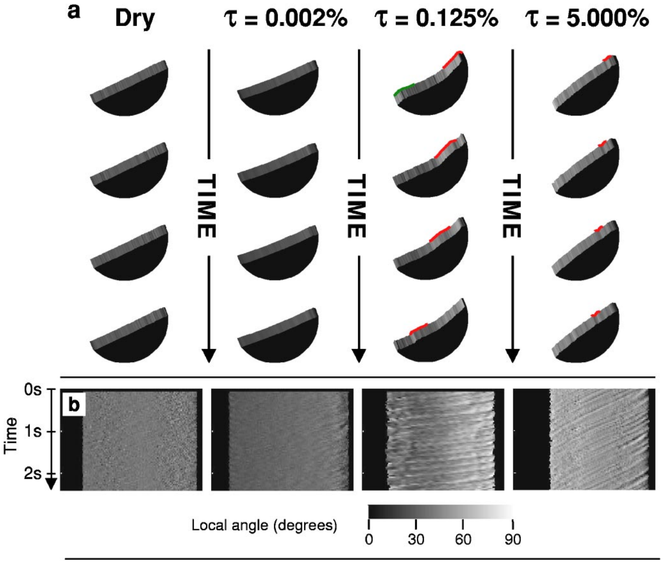

FIG. 21. (Color online) Comparison of the types of continuous flow at $\Omega = 10$ rpm (large beads: $d = 0.9$ mm). (a) Snapshots at time intervals of 0.067 sec. The red marks indicate traveling surface features. (b) Time evolution of the surface angle $\alpha(x,t)$. The traveling surface features appear as stripes.

In order to compare the viscoplastic flow to the ordinary granular flow, we added some tracer particles to measure the surface velocity v more accurately as a function of rotation rate Ω (Fig. 22). The viscoplastic flow is slower by about a factor of 2 than the granular one. More importantly, the two curves correspond to rather different functional forms—both apparently power laws in our limited velocity range, but with different exponents. The sublinear rotation rate dependence in the granular regime suggests that at higher rotation rate the flow depth is increased, as has been previously suggested [48]. Naturally, in our finite setup, the flow depth cannot increase infinitely which may explain why our measured

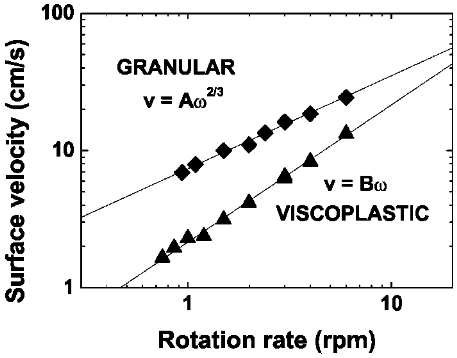

FIG. 22. The velocity v at the surface as a function of rotation rate Ω for the ordinary granular and the viscoplastic continuous flow (large beads, $d = 0.9$ mm, the liquid contents are $\tau = 0.005\%$ and $\tau = 0.25\%$, respectively). The continuous lines represent power-law fits to the data. The linear rotation rate dependence for the viscoplastic flow indicates that flow depth is independent of the rotation rate.

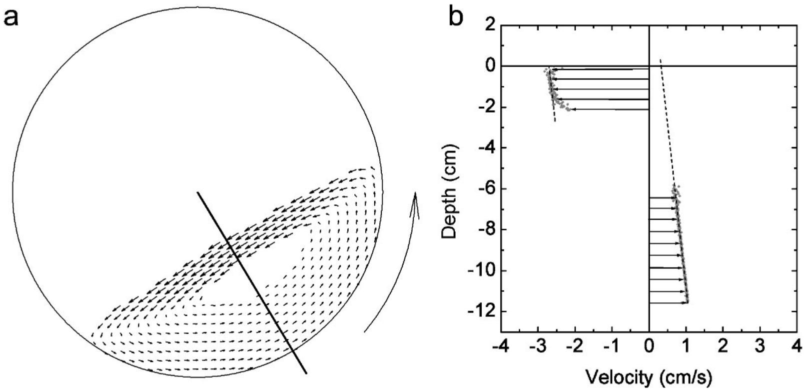

FIG. 23. (a) Velocity field of the viscoplastic flow as obtained by tracer particles. The central region is empty due to lack of data in this region. The actual resolution is much better than the separation of the arrows—the only part of the data is presented for clarity. (b) Velocity profile along the solid line in (a). The diamonds are experimental data, dashed lines correspond to no shear strain. The arrows are only for illustration. ($d=0.9$ mm, $\tau=0.25\%$, $\Omega=0.6$ rpm.)

$v(\Omega)$ deviates from $\Omega^{1/2}$, which would be expected from a linear velocity profile [48–50]. On the other hand, the recent work of Aranson *et al.* actually predicts a 2/3 power law [51,52]. The linear $v(\Omega)$ for viscoplastic flow suggests a *constant flow depth* that is independent of the flow rate. This observation is consistent with the coherent nature of this type of flow: the flow depth is not determined by local mechanisms [14], but is fixed by the geometry of the whole system. In order to characterize the viscoplastic flow in greater detail and check whether the flow depth is really constant, we have performed explicit measurements to determine the extent and shape of the flowing layer. The results confirmed that the flow depth is almost independent of the rotation rate [24].

One of the most interesting properties describing the dynamics of granular flows is the velocity profile, i.e., the depth dependence of the velocity of the particles. We obtained a qualitative picture of the depth dependence of the grain velocity based on tracer particle measurements near the sidewalls. As in any three-dimensional system, the velocity distribution at the sidewalls may be different from velocities in the bulk. This is especially true for wet samples, where the beads adhere to the walls. As a validity check, we examined video recordings of the top surface during flow, which showed that the flow velocity is approximately constant across the width of the drum (32 mm), except for a thin (2–3 mm) boundary layer at each wall. In order to measure velocities a few millimeters behind the walls, we added colored tracer particles to the system (red plastic cubes with a linear size around 3 mm), which were detectable even behind a few layers of glass beads. Lasting contacts in this type of flow ensured that the tracers had the same velocity as the surrounding beads. Naturally, the data may be affected by segregation effects and the modification of flow dynamics by the presence of the tracers, and therefore they should be interpreted with caution.

In Fig. 23, we present the obtained velocity field. In Fig. 23(a), the velocities are represented by little arrows with length proportional to the magnitude of measured velocities. Each arrow represents the average of measured values in a small rectangular area around the starting point of the arrow. Unfortunately, the tracers did not enter the area near the center of the sample, so we have no data from this region. Figure 23(b) presents the measured velocities along the solid line in Fig. 23(a). The points near the bottom of the figure correspond to the tracers that are at rest with respect to the drum and travel only due to the rotation of the drum. In the top region, the material clearly flows with respect to the drum. Interestingly, in an approximately 1.5-cm-thick layer, the observed velocities of the particles differ only due to the rotation of the drum, the particles are at rest with respect to each other. In other words, there is a layer with no shear strain (often referred to as the "plug layer") near the surface of the sample. This phenomenon is due to the vicoplasticity of the material [53].

VIII. CONCLUSIONS

We have investigated many features of the dynamic behavior of wet granular samples in a rotating drum reflecting the three fundamental regimes of behavior observed earlier [12]. In the granular regime, the cohesive forces are relatively small, and they have almost no effect in the fluidized flowing layer. Thus, only a small increase is observable in $\theta_{\max}$, while θ_r hardly changes. The grains are rolling freely, and avalanche dynamics is dominated by propagating fronts. These form nearly flat surfaces resulting in relatively small avalanche size fluctuations. At high rotation rates, we observe continuous flow with a fluidized flowing layer, similar to surface flows in dry samples.

On the other hand, in the correlated regime, the grains stick together and form clumps. The increased cohesion leads to a large increase in $\theta_{\max}$ and θ_r. As the free rolling of grains becomes impossible, the avalanche fronts disappear and steep, rugged, and usually concave surfaces are formed. Variations of the surface shape lead to wide avalanche size distributions. In this regime, the continuous flow consists of a succession of falling clumps, thus the hysteresis between avalanching and continuous flows disappears.

Finally, in the viscoplastic regime, the flow becomes coherent over the entire sample, and $\theta_{\max}$ and $\Delta\theta$ decrease slightly due to lubrication and viscous effects. The reduced fluctuations lead to narrower avalanche size distributions and the formation of robust patterns that are reproduced at the end of each avalanche. The transition to continuous flow happens at relatively low rotation rates, and the hysteresis reappears. The coherence of the viscoplastic continuous flow is manifested in traveling surface features and a velocity independent flow depth.

While the flows we observe appear to have analogies with geophysical events, it is important to note that real geophysical materials usually consist of polydisperse irregular particles often with very high ($\tau \approx 100\%$) water contents and that the scaling of our system to geological length scales is nontrivial (indeed, based our on earlier work we expect that all of the results will be affected by the size of the container [12]). Furthermore, avalanche studies in real soil have demonstrated additional phenomena associated with soil saturation [54]. Interestingly, we still recover some of the basic dynamic processes in our model system, which should aid the description of qualitatively different flow behaviors in the framework of a single model [22,55].

The changes in the dynamic behavior with wetting are associated with the increasingly coherent nature of the flow, i.e., the formation of coherently moving clusters—clumps—due to the increased cohesion and viscous effects. Within a cluster, local velocity fluctuations should be suppressed, and thus the local granular temperature ($T = \langle v^2 \rangle - \langle v \rangle^2$) should approach zero, but the clusters themselves both form and break apart during an avalanche process in a finite container. An important theoretical question raised by our data is that how a length scale describing the size of the clumps may emerge from a granular flow model, and how such a length scale would vary with the type of media, the total size of the granular sample, the nature of intergranular adhesion, viscosity of the fluid, and the type of granular flow. While the present experiments have raised these questions, further experimental studies expanding the investigated phase space as well as computational modeling will almost certainly be necessary before a complete understanding is approachable.

ACKNOWLEDGMENTS

We gratefully acknowledge helpful discussions with J. Banavar, A.-L. Barabási, and Y. K. Tsui. We are also grateful for support from the Petroleum Research Fund and NASA Grant No. NAG3-2384. P.T. and T.V. are grateful for the partial support from OTKA Grant No. T033104.

[1] J.M. Georges, in *Physics of Granular Media*, edited by D. Bideau and J. Dodds (Nova Science, New York, 1991), p. 113.

[2] J.N. Israelachvili, *Intermolecular and Surface Forces* (Academic Press, London, 1985).

[3] R.M. Nedderman, *Statics and Kinematics of Granular Materials* (Cambridge University Press, Cambridge, 1992).

[4] R. Albert, I. Albert, D. Hornbaker, P. Schiffer, and A.-L. Barabási, Phys. Rev. E **56**, R6271 (1997).

[5] D.J. Hornbaker, R. Albert, I. Albert, A.-L. Barabási, and P. Schiffer, Nature (London) **387**, 765 (1997).

[6] T.C. Halsey and A.J. Levine, Phys. Rev. Lett. **80**, 3141 (1998).

[7] T.G. Mason, A.J. Levine, D. Ertas, and T.C. Halsey, Phys. Rev. E **60**, 5044 (1999).

[8] L. Bocquet, E. Charlaix, S. Ciliberto, and J. Crassous, Nature (London) **396**, 735 (1998).

[9] N. Fraysse, H. Thomé, and L. Petit, in *Powders & Grains 97*, edited by R.P. Behringer and J.T. Jenkins (Balkema, Rotterdam, 1997).

[10] A. Samadani and A. Kudrolli, Phys. Rev. Lett. **85**, 5102 (2000).

[11] A. Samadani and A. Kudrolli, Phys. Rev. E **64**, 051301 (2001).

[12] P. Tegzes, R. Albert, M. Paskvan, A.-L. Barabási, T. Vicsek, and P. Schiffer, Phys. Rev. E **60**, 5823 (1999).

[13] P. Tegzes, T. Vicsek, and P. Schiffer, Phys. Rev. Lett. **89**, 094301 (2002).

[14] J. Rajchenbach, Phys. Rev. Lett. **88**, 014301 (2002).

[15] A. Daerr and S. Douady, Nature (London) **399**, 241 (1999).

[16] G.A. Held, D.H. Solina, D.T. Keane, W.J. Haag, P. Horn, and G.G. Grinstein, Phys. Rev. Lett. **65**, 1120 (1990).

[17] P.-A. Lemieux and D. Durian, Phys. Rev. Lett. **85**, 4273 (2000).

[18] L.C. Jia, P.-Y. Lai, and C.K. Chan, Physica A **281**, 404 (2000).

[19] J. Rajchenbach, Phys. Rev. Lett. **65**, 2221 (1990).

[20] C. Liu, H.M. Jaeger, and S.R. Nagel, Phys. Rev. A **43**, 7091 (1991).

[21] N. Fraysse, H. Thomé, and L. Petit, Eur. Phys. J. B **11**, 615 (1999).

[22] S.T. Nase, W.L. Vargas, A.A. Abatan, and J.J. McCarthy, Powder Technol. **116**, 214 (2001).

[23] M.A.S. Quintanilla, J.M. Valverde, A. Castellanos, and R.E. Viturro, Phys. Rev. Lett. **87**, 194301 (2001).

[24] P. Tegzes, Ph.D. thesis, Eötvös University, Budapest 2002, http://angel.elte.hu/~tegzes/thesis.html

[25] S. Nasuno, A. Kudrolli, and J.P. Gollub, Phys. Rev. Lett. **79**, 949 (1997).

[26] I. Albert, P. Tegzes, B. Kahng, R. Albert, J. Sample, M. Pfeifer, A.-L. Barabasi, T. Vicsek, and P. Schiffer, Phys. Rev. Lett. **84**, 5122 (2000).

[27] I. Albert, P. Tegzes, R. Albert, J.G. Sample, A.-L. Barabási, T. Vicsek, B. Kahng, and P. Schiffer, Phys. Rev. E **64**, 031307 (2001).

[28] R.G. Cain, N.W. Page, and S. Biggs, Phys. Rev. E **64**, 016413 (2001).

[29] P. Bak, C. Tang, and K. Wiesenfeld, Phys. Rev. Lett. **59**, 381 (1987).

[30] M. Bretz, J.B. Cunningham, P. Kurczynski, and F. Nori, Phys. Rev. Lett. **69**, 2431 (1992).

[31] V. Frette, K. Christensen, A. Malthe-Sϕrenssen, J. Feder, T. Jϕssang, and P. Meakin, Nature (London) **379**, 49 (1996).

[32] P. Evesque, Phys. Rev. A **43**, 2720 (1991).

[33] G. Baumann and D.E. Wolf, Phys. Rev. E **54**, R4504 (1996).

[34] W. Losert, J.-C. Géminard, S. Nasuno, and J.P. Gollub, Phys. Rev. E **61**, 4060 (2000).

[35] C. Caponeri, S. Douady, S. Fauve, and S. Laroche, in *Mobile Particulate Systems*, edited by E. Guazelli and L. Oger (Kluwer Academic, Dordrecht, 1995), p. 331.

[36] H.M. Jaeger, C. Liu, and S.R. Nagel, Phys. Rev. Lett. **62**, 40 (1989).

[37] V.G. Benza, F. Nori, and O. Pla, Phys. Rev. E **48**, 4095 (1993).

[38] A.D.C. Smith, P.G. Batchelor, X.A. Chitnis, D.L.G. Hill, and T. Sharma, Schizophr Res. **41**, A217 (2001).

[39] S. Douady, B. Andreotti, and A. Daerr, Eur. Phys. J. B **11**, 131 (1999).

[40] S. Douady, B. Andreotti, A. Daerr, and P. Clade, in *Powders & Grains 2001*, edited by Kishino (Swets & Zeitlinger, Lisse, 2001), pp. 443–446.

[41] H.A. Makse, S. Havlin, P.R. King, and H.E. Stanley, Nature (London) **386**, 379 (1997).

[42] J.M.N.T. Gray and Y.C. Tai, in *Physics of Dry Granular Media*, edited by H.J. Herrmann, J.-P. Hovi, and S. Luding (Kluwer Academic, Dordrecht, 1998), pp. 697–702.

[43] P. Cizeau, H.A. Makse, and H.E. Stanley, Phys. Rev. E **59**, 4408 (1999).

[44] R. Dikau, D. Brunsden, L. Schrott, and M.-L. Ibsen, *Landslide Recognition* (Wiley, Chichester, 1996).

[45] R.M. Iverson, Rev. Geophys. **35**, 245 (1997).

[46] P. Coussot, *Mudflow Rheology and Dynamics* (Balkema, Rotterdam, 1997).

[47] D.M. McClung and P. Schaerer, *The Avalanche Handbook* (Mountaineers, Seattle, 1993).

[48] D. Bonamy, B. Faucherand, M. Planelle, F. Daviaud, and L. Laurent, in *Powders & Grains 2001* (Ref. [40]), pp. 463–466.

[49] J. Rajchenbach, in *Physics of Dry Granular Media*, edited by H.J. Herrmann, J.-P. Hovi, and S. Luding (Kluwer Academic, Dordrecht, 1998).

[50] K. Yamane, M. Nakagawa, S.A. Altobelli, T. Tanaka, and Y. Tsuji, Phys. Fluids **10**, 1419 (1998).

[51] I.S. Aranson and L.S. Tsimring, Phys. Rev. E **65**, 061303 (2002).

[52] I. Aranson (private communication).

[53] A.M. Johnson, *Physical Processes in Geology* (Freeman, San Francisco, 1970).

[54] R.M. Iverson, M.E. Reid, N.R. Iverson, R.G. LaHusen, M. Logan, J.E. Mann, and D.L. Brien, Science **290**, 513 (2000).

[55] J.M.N.T. Gray, J. Fluid Mech. **441**, 1 (2001).